Numerical modeling and incoherent Thomson scattering measurements of a 5A cathode with LaB 6 emitter

Laurent Garrigues, Gaétan Sary, Benjamin Vincent, Sedina Tsikata, Stéphane Mazouffre

Numerical modeling and incoherent Thomson scattering measurements of a 5A cathode with LaB_6 emitter

IEPC-2019-783

Presented at the 36th International Electric Propulsion Conference
University of Vienna, Austria
September 15-20, 2019

Laurent Garrigues* and Gaëtan Sary†
Université de Toulouse, CNRS, INPT, UPS, 118 route de Narbonne, 31062 Toulouse cedex 9, France

Benjamin Vincent‡ and Sedina Tsikata§ and Stéphane Mazouffre¶
ICARE, UPR 3021 CNRS, Orléans, France

Emissive cathodes serve as the electron source for Hall plasma thrusters, needed to maintain the ionization region, and also to act as neutralizers for the accelerated ions in these devices. As they are currently the lifetime-limiting components of thrusters, reliable and robust numerical modeling of their operation is key. In this paper, results from the application of a recently-developed 2D axisymmetric fluid code to the modeling of a 5A LaB_6 emissive cathode are presented. These results are compared with new electron property measurements obtained via a recently-developed incoherent Thomson scattering diagnostic. Good agreement between numerical and experimental results are found, as well as an interesting dependency of the code results to the LaB_6 emitter temperature.

Nomenclature

n_n	= neutral density
n	= plasma density
T_e, T_i, T_n	= electron, ion, neutral temperature
k_{io}	= ionization rate coefficient
$\mathbf{u_n}, \mathbf{u_i}$	= neutral, ion velocity
$\mathbf{j_e}, \mathbf{j_i}$	= electron, ion current density
M, m	= xenon ion mass, electron mass
e	= elementary charge
Φ	= plasma potential
ν_e	= electron collision frequency
ν_{iso}	= isotropic neutral collision frequency
$\lambda_n, \lambda_i, \lambda_e$	= neutral, ion and electron thermal conductivities
$k^m_{\alpha,s}$	= momentum exchange collision rate between species α and s
$k^i_{\beta,s} n$	= inelastic collsion rate for species s and a collision process β

*Director of Research, GREPHE, LAPLACE, laurent.garrigues@laplace.univ-tlse.fr
†PhD student, GREPHE, LAPLACE, sary@laplace.univ-tlse.fr
‡PhD student, Electric Propulsion Team, benjamin.vincent@cnrs-orleans.fr
§Researcher, Electric Propulsion Team, sedina.tsikata@cnrs-orleans.fr
¶Director of research, Electric Propulsion Team, stephane.mazouffre@cnrs-orleans.fr

I. Introduction

Research into the operation modes and design optimization of emissive cathodes for thrusters has been ongoing for the past several decades.[1–3] Recent work concerns not only cathodes in the high-current (100 A) range, destined for thruster powers of several tens of kW,[4,5] but also low-power designs[6] for miniature thrusters, suitable for micro- and nanosatellite applications.

Concerted efforts have been devoted to the study of the crossed-field discharge of the main Hall thruster plume, allowing the analysis of the diverse phenomena, including the excitation of plasma waves potentially affecting thruster operation.[7] The development of alternative thruster architectures using magnetic shielding[8] provides a means of extending thruster lifetimes significantly. However, cathode physics has proven to be surprisingly complex. Emissive cathodes are subject to bombardment and erosion by accelerated ions, a phenomenon which appears to be linked to the development of ion acoustic turbulence in the cathode plume,[9] and are as such the lifetime-limiting component of thrusters. The nature of the coupling between the emissive cathode plume and the main thruster plume is another topic requiring further investigation, particularly as it may affect global features such as discharge oscillations. The ability to understand such aspects requires advanced cathode codes.

In recent work, we have developed a 2D axisymmetric fluid model[10,11] for the simulation of cathode thermal and plasma physics. This model, applied to the NSTAR NASA cathode, proved capable of accurately reproducing profiles for the interior and exterior electron properties measured using probes. Electrostatic probes, however, have clear limitations, even when applied to the investigation of unmagnetized plasma sources. In this work, we apply the fluid model to a 5A MIREA LaB_6 cathode in a range of operating regimes, and compare these results with new incoherent Thomson scattering measurements on this cathode. These results provide a means for evaluating the code performance, and provide reliable measurements of electron properties using a non-invasive diagnostic.

II. Cathode details and operation

The cathode considered in this work is based on the model developed by the Russian MIREA institute and features a thermo-emissive LaB_6 pellet heated by a tungsten filament to eject electrons. The experimental setup uses a stainless steel disc anode of diameter 110 mm with a central hole of diameter 21 mm to establish the potential drop through which the electrons are accelerated. This anode faces the 3 mm-diameter cathode orifice and is located at an axial distance of 40 mm. The production of electrons sustains the cathode (xenon) discharge. Fig. 1 shows the basic architecture of this cathode. The cathode is operated over a range of heating currents (2 - 16 A) and flow rates (0.2 - 0.8 mg/s).

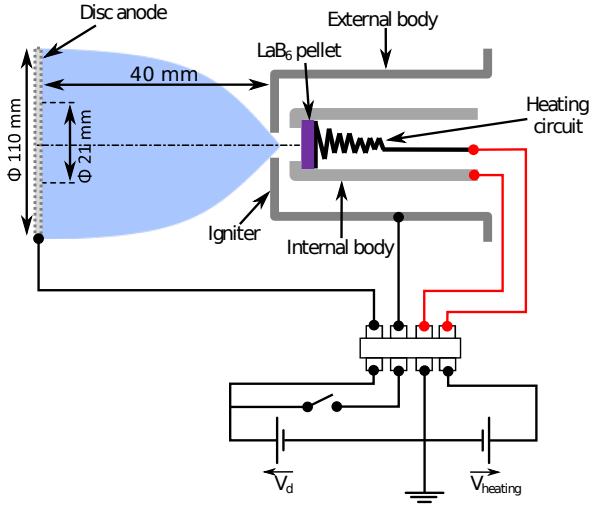

Figure 1. Diagram of MIREA cathode architecture and electrical connections. The cathode is operated without a thruster, with an external disc anode. The plasma region is shown in blue.

III. Incoherent Thomson Scattering experiments

A. Summary of diagnostic principles and features

Electron property measurements were performed using the recently-developed incoherent Thomson scattering diagnostic THETIS.[12] To increase its sensitivity, this diagnostic uses a recently-developed volume Bragg grating notch filter to limit stray light transmission near the incident laser wavelength, and allows a higher transmission efficiency outside the band-stop region and a simpler detection branch in comparison to diagnostics using triple grating spectrometers. Further information about the bench design can be found elsewhere.[12]

The diagnostic setup is shown in Fig. 2. The diagnostic setup is composed of a transmission branch used to produce the Thomson scattering signal (in dark green in Fig. 2) and the detection branch used to collect scattered light over a reduced solid angle, filter stray light and spectrally disperse and measure the scattered signal (in light green in Fig. 2).

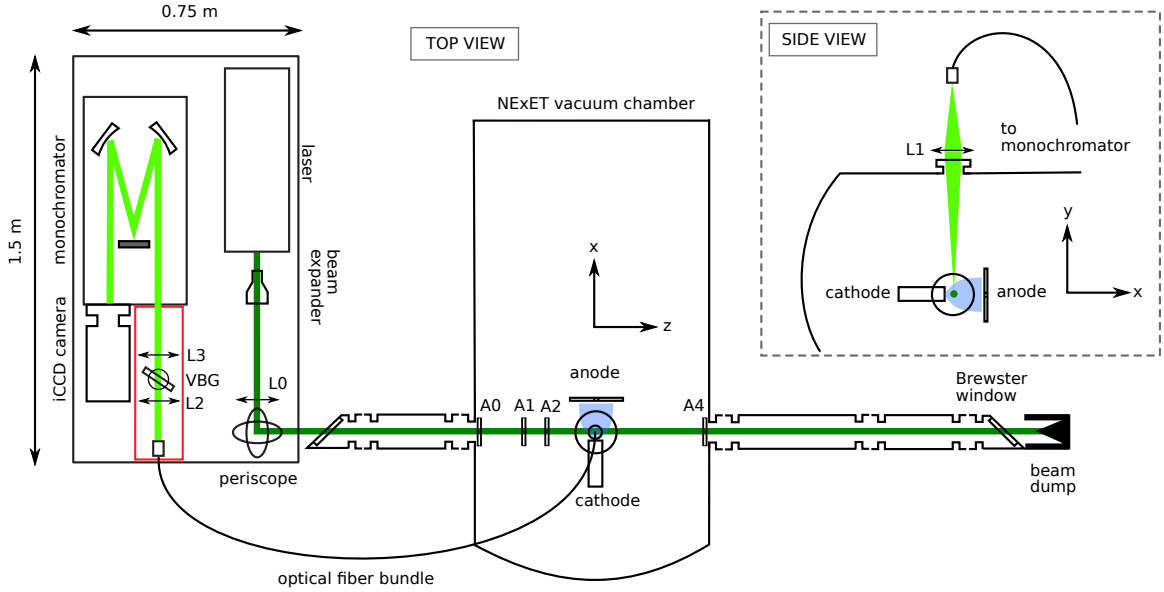

Figure 2. View of the THETIS incoherent Thomson scattering bench setup (not to scale). Two views are shown: a top view of the bench and laser beam trajectory (in dark green) and a side view, showing the collection of scattered light (in light green) at the top of the vacuum vessel. $L0$**,** $L1$**,** $L2$**, and** $L3$ **indicate lenses;** $A0$**,** $A1$**,** $A2$**, and** $A3$ **indicate apertures;** $VBG - NF$ **indicates the volume Bragg grating notch filter used for Rayleigh and stray light suppression.**

The light source of the transmission branch is a 10 Hz pulsed, frequency-doubled Q-switch Nd:YAG laser (λ_0 = 532 nm; E_{pulse} = 430 mJ; τ_{pulse} = 5 ns. The initial vertically polarized 9 mm diameter beam is expanded with a magnification of 3 and focused with a 2m-focal length lens in the plasma volume. To reduce stray-light propagation the beam passesthrough two Brewster windows mounted at the end of tubes inside which apertures are placed. The beam ends its path in a large-aperture beam dump.

Scattered light is collected and imaged onto the entrance of a 5 × 3 matrix of fibers (0.3 mm in individual diameter) with a 200 mm focal length lens. The fiber bundle conducts the light to the optical bench where it is collimated, filtered by the notch filter, and transmitted to the spectrometer. An intensified camera is triggered on the laser Q-switch signal to detect scattered photons. The procedures adopted for signal detection and calibration are presented in Ref.[12] This diagnostic has a high enough sensitivity for application to plasma environments with densities as low as 10^{16} /m^3.

Examples of Thomson spectra obtained from cathode experiments for two different discharge currents are shown in Fig. 3, with corresponding electron properties in the caption. From these spectra, electron temperature (deduced from the spectral width) and density (deduced from the spectrum area) are determined. These spectra show the region of rejected data (due to presence of the stray light filter, in orange), the full set of experimental points from these spectra (in blue) and the green fit line from which Gaussian fit parameters are determined to deduce the electron properties. As is clear from Fig. 3(a), the high sensitivity

of this diagnostic allows detection of Thomson signal amplitudes of only a few counts.

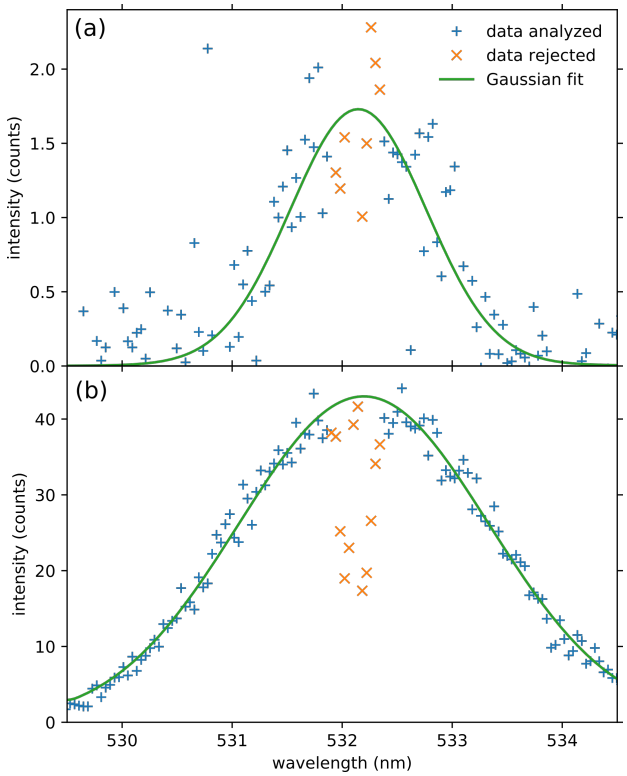

Figure 3. Examples of cathode Thomson spectra illustrating the diagnostic sensitivity. These examples, measured 6 mm from the cathode orifice, correspond to (a) 2A discharge current, T_e 0.5 ± 0.05 eV; n_e = 2 ± 0.2 × 10^{16} /m3 and (b) 16 A discharge current, 1.2 ± 0.1 eV; n_e = 9.5 ± 0.8 × 10^{17} /m^3.

IV. Numerical model

A. Governing equations

Full details on the numerical method are presented in Ref.,[10] and are only briefly summarized here. The numerical scheme used considers three species: Xe atoms, Xe+ ions and electrons, with multiply-charged ions neglected. Maxwellian velocity distributions are considered to apply for all species in this plasma. Inside the cathode, the transport of species is dominated by collisions between electrons and neutrals (e–n), between ions and neutrals (i–n), and Coulomb collisions between electrons and ions (e–i). The plasma is assumed to be quasi-neutral.

The main governing equations are:

(i) the mass conservation equations for the neutrals and ions:

$$\frac{\partial n}{\partial t} + \nabla \cdot (n\mathbf{u_i}) = S \tag{1}$$

$$\frac{\partial n}{\partial t} + \nabla \cdot (n\mathbf{u_i}) = -S \tag{2}$$

with $n = n_i = n_e$ and the source term $S = nn_n k_{io}(T_e)$ for the rate coefficient k_{io}

(ii) the momentum conservation equations for Xe+ ions, neglecting viscosity and magnetic field:

$$M\left(\frac{\partial}{\partial t}(n\mathbf{u_i}) + \nabla \cdot (n\mathbf{u_i} \otimes \mathbf{u_i})\right) = -ne\nabla\Phi - \nabla p_i + MS\mathbf{u_n} \tag{3}$$

(iii) the electron drift diffusion equation:

$$\mathbf{j_e} = -en\mu_e \nabla\Phi + \mu_e \nabla p_e \tag{4}$$

with the electron pressure $p_e = nk_BT_e$ and the electron mobility $\mu_e = e/m\nu_e$,
(iv) charge conservation:

$$\nabla \cdot (\mathbf{j_i} + \mathbf{j_e}) = 0 \tag{5}$$

giving the expression for the plasma potential

$$\nabla \cdot (en\mu_e \nabla\phi) = \nabla \cdot (\mu_e \nabla p_e + en\mathbf{u_i}) \tag{6}$$

(v) and lastly, energy conservation:

ions:

$$\begin{aligned} \frac{\partial}{\partial t}\left(\frac{3}{2}p_n\right) + \nabla \cdot \left(\frac{5}{2}p_n\mathbf{u_n} + \mathbf{q_n}\right) &= \mathbf{u_n} \cdot \nabla p_n - \frac{3}{2}k_BT_nS - \mathbf{u_s} \cdot \nabla \cdot \mathbf{T} \\ + \nabla \cdot (\mathbf{T}\mathbf{u_s}) + Q_n - (\mathbf{R}_{iso,i} + \mathbf{R}_{e\to n}) \cdot \mathbf{u_n} & \end{aligned} \tag{7}$$

where $Q_n = n\bar{n}u_{iso}k_B(T_i - T_n) + 3\frac{m}{M}nn_nk^m_{e,n}k_B(T_e - T_n)$ and the neutral thermal conduction flux is $\mathbf{q_n} = -\lambda_n \nabla T_n$.

ions:

$$\begin{aligned} \frac{\partial}{\partial t}\left(\frac{3}{2}p_i\right) + \nabla \cdot \left(\frac{5}{2}p_i\mathbf{u_i} + \mathbf{q_i}\right) &= \mathbf{u_i} \cdot \nabla p_i + Q_i - (\mathbf{R}_{iso,n\to i} + \mathbf{R}_{e\to i}) \cdot \mathbf{u_n} \\ + \frac{3}{2}k_BT_nS + \frac{1}{2}MS(\mathbf{u_i} - \mathbf{u_n})^2 & \end{aligned} \tag{8}$$

where $Q_i = n\nu_{in}k_B(T_n - T_i) + 3\frac{m}{M}n\nu_{ie}k_B(T_e - T_i)$ and $\mathbf{q_i} = -\lambda_i \nabla T_i$,

electrons:

$$\frac{\partial}{\partial t}\left(\frac{3}{2}p_e\right) + \nabla \cdot \left(\frac{5}{2}p_e\mathbf{u_e} + \mathbf{q_e}\right) = \mathbf{u_e} \cdot \nabla p_e + Q_e + m\nu_e n\mathbf{u_e}^2 - S\epsilon_{io} \tag{9}$$

where $Q_e = 3\frac{m}{M}n\nu_{ie}k_B(T_i - T_e) + 3\frac{m}{M}nn_nk^m_{e,n}k_B(T_n - T_e)$ and $\mathbf{q_e} = -\lambda_e \nabla T_e$.

B. Simulation domain

The existing simulation domain is adapted to match that of the MIREA cathode under study. Fig. 4 shows the mesh with respect to the cathode dimensions and architecture. The figure shows the simulation domain applied to half of the axisymmetric cathode, along with the dimension and placement of the anode (blue) and LaB_6 emitter (red).

The plasma simulation domain is discretized using a Cartesian mesh of 1880 nodes (710 in the internal region of the cathode). Further details on the discretization method are provided in Ref. 10. The mesh is finest between the emitter and the orifice with a square cell size of 0.215 mm. A similar mesh has been used for the thermal domain.

V. Results from 2D simulation

A. Simulation parameter variations

The 2D fluid model was used to simulate the discharge at identical discharge conditions to those explored by ITS. Because the temperature of the LaB_6 emissive pellet is a key parameter for the simulation, and one whose measurement with high precision is challenging, a study of its influence on the electron density and temperature values outside the cathode has been performed. The temperature of the pellet was chosen close

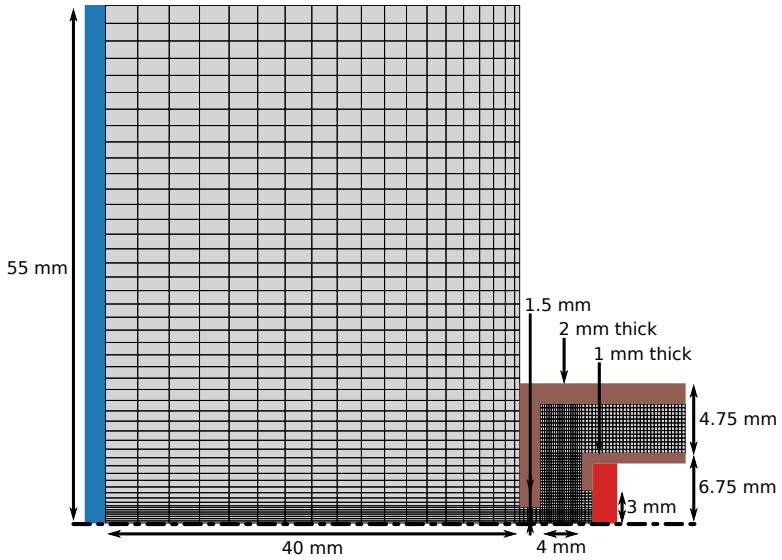

Figure 4. Simulation region analyzed with the fluid code to match MIREA architecture. The disc anode is shown in blue, and the LaB_6 emitter in red.

to values previously measured in our team with a thermocouple. The temperature was then varied by 5 K steps over a dynamic of 100 K (where possible) around the expected value. Discharge currents from 2 to 16 A with a xenon flow rate of 0.8 mg/s were simulated.

For each set of discharge parameters simulated, the simulation was run during 5 ms, and convergence was verified. Electron temperature and density were extracted from a temporal average over the last 1 ms of simulation and from a spatial average over the radial length probed by the detection branch in scattering experiments (up to 1.2 mm from the cathode axis). The axial profiles for a selected set of emissive pellet temperatures are shown in 5 at 2 and 8 A. The set of emissive pellet temperatures displayed was chosen in order to maximize readability on the figures.

Some general trends apply to both discharge currents shown in Fig. 5. The electron density always decreases monotonically with increased distance from the cathode orifice. When the temperature of the emissive pellet is increased, electron density outside the cathode orifice progressively decreases before reaching a steady low-density profile at high emissive pellet temperature.

The trend in electron temperature changes as the emissive pellet temperature rises. For the presented results, electron temperature decreases with distance from the orifice at low emissive pellet temperature. However, at higher emissive pellet temperatures, the electron temperature first increases at distances close to the cathode orifice before approaching a plateau (visible for 8A). The position at which this plateau starts to develop becomes closer to the orifice as emitter temperature increases. For the 8 A, 0.8 mg/s discharge conditions, the transition from a low T_e, high n_e regime at low emissive pellet temperature to a high T_e, low n_e regime at higher pellet temperature may correspond to a transition from the spot mode of operation to a plume mode, if we consider electron density and temperature values as the criteria for judging such a mode transition.

VI. Comparisons between scattering data and simulations

Several comparisons have been performed at different operating points within the range 2 - 16 A of discharge currents used for the cathode, at different flow rates. The example discussed in this section is selected to illustrated more general observations.

Fig. 6 shows the electron density and temperature profiles from the simulation at 8 A and flow rate of 0.8 mg/s, for two different La_6 emitter temperatures. The experimentally-determined values are shown in red. The choice of two emitter temperatures for the comparisons is deliberate. At 2050 K, we observe a good agreement between the simulation electron density profile and that determined experimentally. The trend and absolute values are very similar for both. However, the agreement for the electron properties is quite

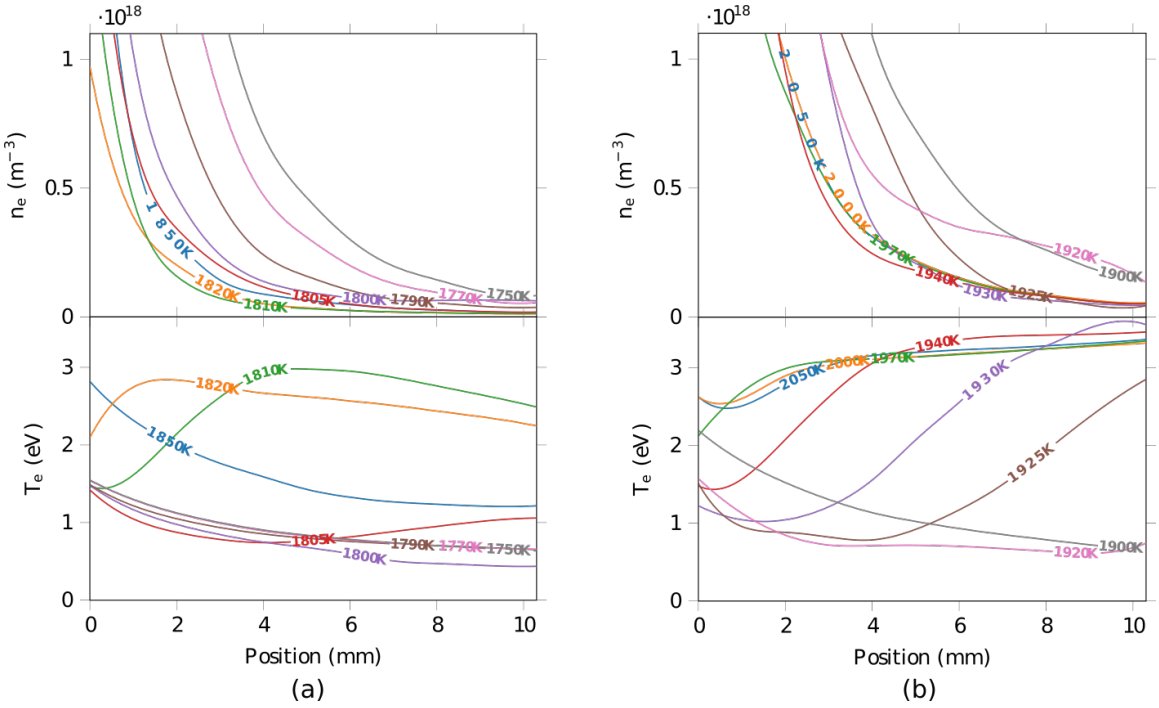

Figure 5. Examples of simulated electron density and temperature for (a) 2A discharge current and 0.8 mg/s flow rate with LaB_6 emitter temperature varied from 1750 - 1850 K, and (b) 8A discharge current and 0.8 mg/s flow rate with LaB_6 emitter temperature varied from 1825 - 1925 K

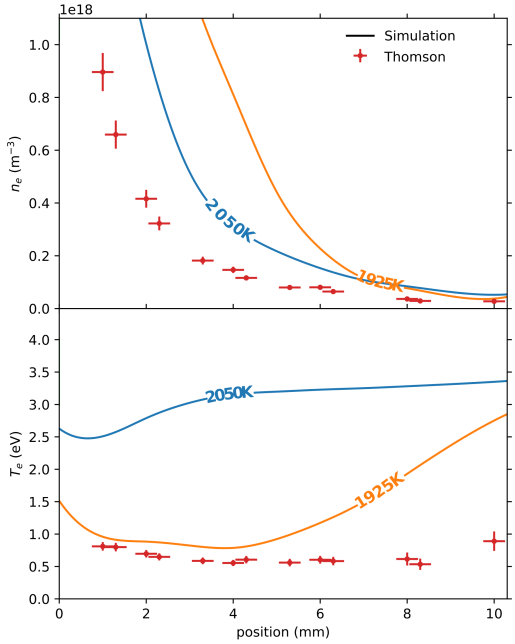

Figure 6. Comparison between electron properties obtained from the simulation (at two different emitter temperatures) and in scattering experiments, for a cathode discharge current of 8 A and flow rate of 0.8 mg/s.

different. Over the axial range explored, the electron properties in the simulation are observed to exceed the experimentally-measured values by about a factor of 3, for this fixed emitter temperature.

Considering another emitter temperature shows a slightly different result. At 1925 K, we observe close agreement in the electron temperatures of the simulation and from the experiments. However, the corresponding densities for a given axial location differ to some degree.

These results illustrate the sensitivity of agreement to the emitter temperature, which is fixed in the simulation. While the agreement (the order of magnitude of the values obtained in simulation, compared to those measured directly) is quite good, it is likely further refinements to the code thermal modeling could improve the match between the simulated and measured properties.

VII. Conclusions

This paper discusses results produced from a recently-developed 2D axisymmetric cathode code applied to the modeling of a 5A MIREA-type cathode with an LaB_6 emitter. The electron properties obtained in a simulation, for different emitter temperatures, are examined, and reveal the dependence of the electron density and temperature trends on the emitter temperature. At one operating point, these results are compared to those directly obtained from incoherent Thomson scattering measurements. It is observed that while the general trends and and order of magnitudes for the electron properties are similar for the simulation and experiments, the emitter temperature influences the agreement. Different values of emitter temperature can produce better agreement for either the electron density or the temperature. This result highlights the importance of the cathode thermal modeling in influencing the code outcomes.

VIII. Acknowledgments

The authors would also like to acknowledge support from CNES and C. Boniface.

IX. References

References

[1]G. A. Csiky. *AIAA 7th Electric Propulsion Conference, Williamsburg, Virginia, March 3 - 5*, 69-258, 1969.

[2]G. A. Csiky. *J. Spacecraft*, 7:474, 1969.

[3]C. M. Philip. *AIAA Journal*, 9:2191, 1971.

[4]D. M. Goebel, R. M. Watkins, and K. K. Jameson. *J. Prop. Power*, 23:552, 2007.

[5]I. G. Mikellides, D. M. Goebel, B. A. Jorns, J. E. Polk, and P. Guerrero. *IEEE Trans. Plasma Science*, 43:173, 2015.

[6]F. Nürmberger, A. Hock, and M. Tajmar. *51st AIAA/SAE/ASEE Joint Propulsion Conference, July 27-29, 2015, Orlando, Florida*, 2015-3822, 2015.

[7]E. Y. Choueiri. *Phys. Plasmas*, 8:1411, 2001.

[8]I. G. Mikellides, I. Katz, R. R. Hofer, and D. M. Goebel. *Appl. Phys. Lett.*, 102:023509, 2013.

[9]B. A. Jorns, I. Mikellides, and D. Goebel. *Phys. Rev. E*, 90:063106, 2014.

[10]G. Sary, L. Garrigues, and J.-P. Boeuf. *Plasma Sources Sci. Technol.*, 26:055007, 2017.

[11]G. Sary, L. Garrigues, and J.-P. Boeuf. *Plasma Sources Sci. Technol.*, 26:055008, 2017.

[12]B. Vincent, S. Tsikata, S. Mazouffre, T. Minea, and J. Fils. *Plasma Sources Sci. Technol.*, 27:055002, 2018.